

# Revealing the role of organic cations in hybrid halide perovskites $\text{CH}_3\text{NH}_3\text{PbI}_3$

Carlo Motta,<sup>1,2,\*</sup> Fedwa El Mellouhi,<sup>2,†</sup> Sabre Kais,<sup>2</sup> Nouar Tabet,<sup>2</sup> Fahhad Alharbi,<sup>2</sup> and Stefano Sanvito<sup>1</sup>

<sup>1</sup>*School of Physics, AMBER and CRANN Institute, Trinity College, Dublin 2, Ireland*

<sup>2</sup>*Qatar Environment and Energy Research Institute, Doha, Qatar*

(Dated: March 17, 2019)

Solar cells based on the hybrid halide perovskite,  $\text{CH}_3\text{NH}_3\text{PbI}_3$ , have now reached an efficiency of about 17%, demonstrating a pace for improvements with no precedents in the solar energy arena. Despite such explosive progress, the microscopic origin behind the success of such material is still debated and in particular it is not clear what role the organic cations play in the light-harvesting process. Here density functional theory calculations including van der Waals interactions reveal that the organic molecules do not contribute directly to the electronic structure close to the bandgap but they play a fundamental role in determining the crystal geometry. The high-temperature cubic phase of  $\text{CH}_3\text{NH}_3\text{PbI}_3$  allows the molecules to assume different high-symmetry configurations within the crystal and, when  $\text{CH}_3\text{NH}_3$  is oriented along the (011) or (0-11) direction, the octahedral  $\text{PbI}_6$  cage distorts. Such distortion is the direct result of van der Waals interactions and has drastic consequences on the electronic structure. Remarkably the bandgap turns from direct to indirect, thus enhancing the lifetime of the charge carriers. Our results suggest possible design strategies for novel high-efficiency hybrid halide perovskites and opens a route for further investigation taking into account the dynamic of the organic cations.

## INTRODUCTION

Very few materials have taken a research field by storm as the hybrid halide perovskites have done in the last eighteen months for the solar cell community<sup>1</sup>. These are compounds with the standard  $\text{AMX}_3$  perovskite structure, where X is the halide iodine, M is lead, while the remaining cation position, A, is taken by an organic molecule, in this case methyl-ammonium,  $\text{CH}_3\text{NH}_3$ . The success of such compounds is that high-efficiency solar cells can be grown cheaply from the liquid phase<sup>2,3</sup> and that the efficiency can be tuned by controlling their structural order and composition<sup>4,5</sup>. Particularly intriguing is the fact that high efficiencies are achieved even for planar cells<sup>6</sup>, indicating that charge separation can occur in the hybrid perovskite absorber and that efficient charge diffusion takes place for both electrons and holes<sup>7</sup>.

Part of this behaviour can be related to the unusual situation concerning possible intrinsic defects. Recent electronic structure calculations<sup>8,9</sup> have shown that the dominant simple or complex defects in  $\text{CH}_3\text{NH}_3\text{PbI}_3$  produce only shallow defect levels, while those able to act as deep traps have a high formation energy. Such observation suggests that, under ideal conditions, deep-level point defects cannot act as non-radiative recombination sites; a fact that can partially explain the relative long exciton lifetimes ( $\tau$ ) and diffusion lengths ( $L_{\text{diff}}$ ) observed in these materials. At the same time the absence of deep levels may explain also the large open-circuit voltage measured. However, despite all these hints many fundamental questions remain open. In particular it is still not clear what is the role played by the organic molecules in the efficiency of these compounds. Theoretical investigations have now built a consensus that the methyl-ammonium (MA) group does not have any significant contribution to the electronic structure around the band edges<sup>8,10,11</sup> and suggest that the only role of

the molecules is that of donating an electron to the Pb-I framework, thus stabilizing the perovskite structure.

Interestingly, not even the geometrical arrangement of the MA group is known in detail. At low temperature (below 150 K) the crystal adopts an orthorhombic ( $Pnma$ ) structure, in which the  $\text{PbI}_6$  octahedra are strongly deformed assuming a rectangular basal plane. Such deformation restricts the rotational degrees of freedom of the MA in the rhombus-shaped interstitial region, thus imposing a spatial ordering to  $\text{CH}_3\text{NH}_3$ . In this case the organic cation is pinned and can only rotate along the C-N axis. As the temperature is increased and the material progressively assumes a cubic structure ( $Pm-3m$ ), by passing through a tetragonal one ( $I4/m$ ), the  $\text{CH}_3\text{NH}_3$  molecules become free to rotate between the octahedral cages. Above room temperature such rotation is fast, to a point where both crystallographic analysis<sup>3,12</sup> and NMR measurements<sup>13</sup> have shown that the exact location of the MA groups cannot be determined.

Here we conduct density functional theory (DFT) calculations for  $\text{CH}_3\text{NH}_3\text{PbI}_3$  in the cubic phase, by taking into consideration the experimentally reported evidence of the fast rotation of  $\text{CH}_3\text{NH}_3$ . This means that we do not limit our analysis to  $\text{CH}_3\text{NH}_3$  oriented along the (100) or (111) direction, for which the high  $O_h$  symmetry is maintained, but we also explore cases where the symmetry is lowered. We find that such symmetry lowering has profound consequences on the electronic structure, namely that the bandgap changes from direct to indirect. Crucially such symmetry-lowering configurations represent local minima in the free energy surface of the crystal and they are stabilized by van der Waals (vdW) interactions. These are the key ingredient not only for obtaining accurate lattice parameters<sup>12,14</sup> but also for the internal geometry. Our calculations then return a picture of the  $\text{CH}_3\text{NH}_3\text{PbI}_3$  as a “dynamical” bandgap semiconductor, in which the exact position of

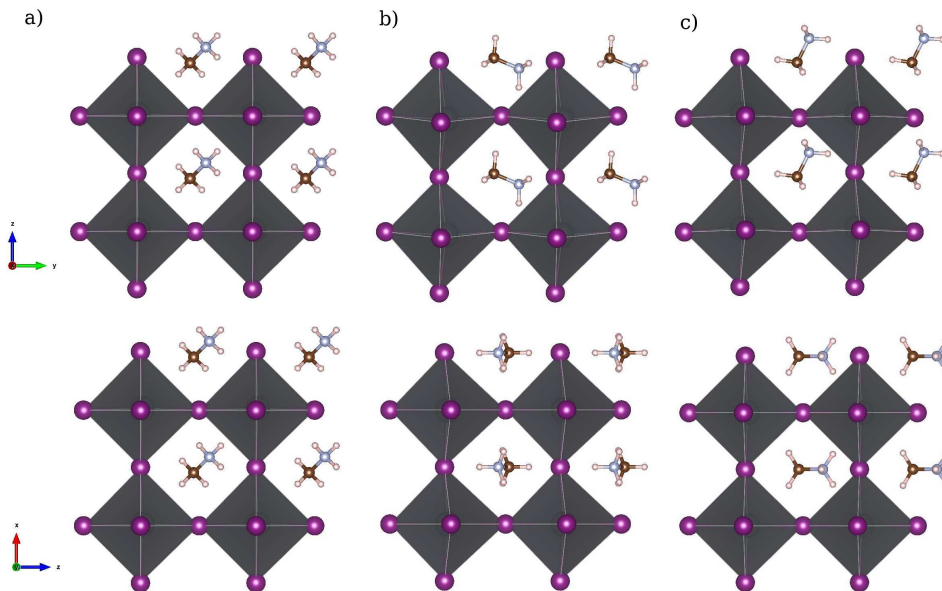


FIG. 1. Relaxed structures of the cubic phase of  $\text{CH}_3\text{NH}_3\text{PbI}_3$  for three different orientations of the cations, namely along (a) (111), (b) (0-11) (b) and (c) (011). The views along the  $xy$  and  $xz$  planes are shown in the upper and lower panels, respectively.

the conduction band minimum depends on the particular spatial arrangement of the molecules. Importantly our results are robust against bandgap corrections and spin-orbit interaction<sup>11,15–18</sup>, and deliver an absorption spectrum in good agreement with experimental data near the absorption edge.<sup>7,19</sup>

## RESULTS

### Geometrical Optimization

Let us start the discussion by presenting the relaxed crystal geometries. Initially all the calculations have been performed at the level of the generalized gradient approximation (GGA)<sup>20</sup> to the DFT exchange and correlation functional, including vdW interactions<sup>21</sup> (see the section computational details) and without explicitly considering spin-orbit coupling. Additional calculations beyond the PBE and with spin-orbit coupling will be discussed later in relation to the electronic structure.

In Fig. 1 the relaxed structures for the cubic phase of  $\text{CH}_3\text{NH}_3\text{PbI}_3$  are presented along the  $xy$  and  $xz$  planes for three different orientations of the  $\text{CH}_3\text{NH}_3$  cation. The relaxation process is extremely sensitive to the initial

conditions. When we start the geometrical optimization with the molecular cation oriented along the (111) direction, the structure relaxes maintaining the same orientation [panel (a)]. In contrast, by starting from a (001) oriented molecule the relaxation may end up with  $\text{CH}_3\text{NH}_3$  either along (0-11) [panel (b)] or (011) [panel (c)]. However, it is important to point out that the cation energy landscape is very shallow. Indeed, all the three configurations represent local energy minima, with an energy difference of only about 20 meV in favor of (011) and (0-11). In all the three cases, the lattice parameters are calculated in excellent agreement with the experimental value of 6.329<sup>22</sup> and an error of less than 0.8% (see SI:Table 1). If one does not include vdW forces in the relaxation, the discrepancy with the nominal value will become larger than 2%, i.e. the crystal structure is not properly described. Furthermore, the molecular bending angle increases from 16° to 25° upon inclusion of dispersion forces. In order to make a well-grounded comparison with previous calculations<sup>11,23</sup> reporting no effect of methyl-ammonium on the structure, we started the relaxation from the experimentally published atomic coordinates with  $\text{CH}_3\text{NH}_3$  along (100)<sup>24</sup> whose band structure is presented in the SI: fig1.

By inspecting the relaxed structures a prominent difference between the (111) and the other two geometries appears. In fact, in the case of (0-11) and (011) the rotation of the cation induces a deformation and symmetry reduction of the inorganic  $\text{PbI}_6$  octahedra. Let us dis-

cuss in detail the (011) geometry, since it is essentially identical, except for the direction, to the (0-11) one. In this case the cause of the distortion of the  $\text{PbI}_6$  octahedra is that the Pb-I bonds do not lie parallel to the crystal directions, but instead they slightly deviate by approxi-

mately  $6^\circ$ . Unlike the (111) case, the unit cell becomes pseudocubic with the lattice parameters along the  $y$  and  $z$  directions being 1% larger than that along  $x$ . Hence, it is clear that the dispersive forces are critical for the internal geometry optimization and, as we will see next, for the electronic behavior of hybrid perovskites.

### Electronic Properties

The fine differences in the crystal geometries have a qualitatively strong impact on the electronic structure. In Fig. 2 we show the electronic bandstructure along the high symmetry points of the Brillouin zone. For all the three cases the energy gap lies in the 1.5-1.7 eV range, close to the experimental value of about 1.55 eV<sup>19,25</sup>. However, as already shown<sup>5</sup>, this agreement is due to a fortuitous cancellation of errors, namely the PBE underestimates the bandgap, but this is counterbalanced by the lack of spin-orbit interaction. It is well known that the bottom of the conduction band mainly originates from the  $p$  orbitals of Pb, while the top of the valence band is derived from the  $p$  orbitals of I. The highest occupied molecular orbital (HOMO) of methyl-ammonium is found deep below the valence band, approximately 5 eV below the valence band maximum (VBM). Thus, one may argue that  $\text{CH}_3\text{NH}_3$  does not play any role in the optical and electronic response of such materials, but that rather it does only contribute to their structural cohesion. However, a careful analysis of the density of states (DOS) projected on the various atoms [see Fig. 3(a) and SI: fig 2] reveals that there is a small contribution  $\sim 0.5$  eV below the VBM attributable to the organic molecules. This indicates that indeed there is interaction between  $\text{CH}_3\text{NH}_3$  and the inorganic  $\text{PbI}_6$  octahedra.

A closer inspection to the bandstructures reveals that the orientation of  $\text{CH}_3\text{NH}_3$  has a profound impact on the nature of the bandgap. In fact, while for the (111) case the gap is direct at the R point, the cationic rotation induces a transition to an indirect gap. In fact the conduction band minimum (CBM) shifts along the  $\text{R} \rightarrow \Gamma$  line for the (0-11) orientation and along the  $\text{R} \rightarrow \text{M}$  one for (011). Accordingly, the vertical energy difference between the CBM and the conduction band energy at R is 25 meV for (0-11) and 95 meV for (011), as shown in the lower panel of Fig. 2.

Such gap transformation is the most remarkable demonstration of the interaction between the organic molecules and the inorganic framework, which is driven by the dispersive forces. In particular,  $\text{CH}_3\text{NH}_3$  exerts strain on the  $\text{PbI}_6$  octahedra and changes the nature of the bandgap. This is unusual in the perovskites world and it is a unique peculiarity of such hybrid systems. Typical inorganic perovskites such as  $\text{SrTiO}_3$  respond to very small uniaxial strains, as those induced by the antiferrodistortive phase transition, by splitting their 3-fold degenerate CBM<sup>26</sup>. To the best of our knowledge very few semiconductors see their bandgap chang-

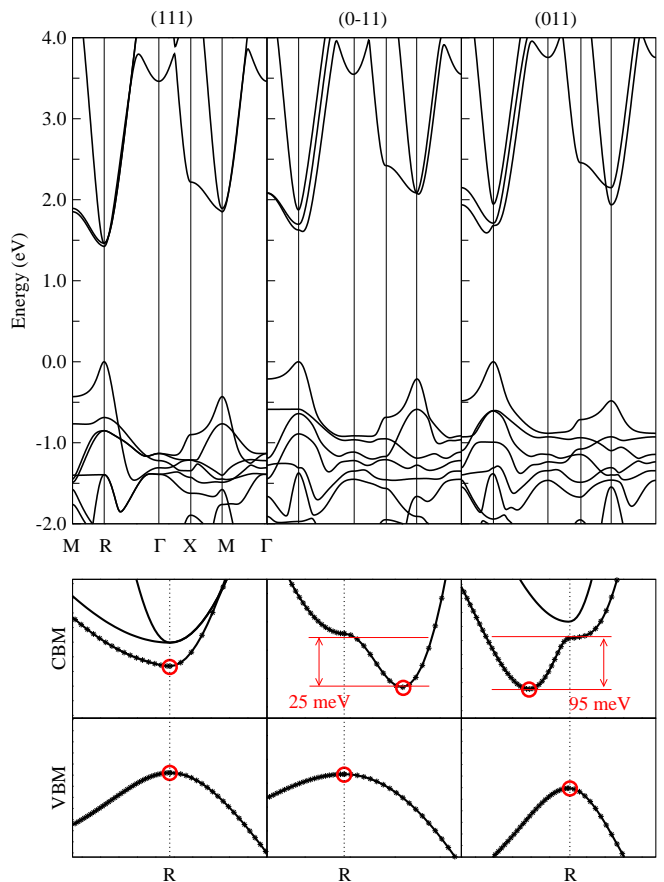


FIG. 2. Band structure of the fully relaxed  $\text{CH}_3\text{NH}_3\text{PbI}_3$  crystal for three different orientation of the organic molecule, namely (a) (111), (b) (0-11) and (c) (011). The lower panel is a magnification of the bands around the bandgap and highlights the changes in the VBM and CBM caused by the rotation of  $\text{CH}_3\text{NH}_3$ . Note that for the (0-11) and (011) orientations the bandgap becomes indirect.

ing from direct to indirect under the effect of strain. An example is given by layered transition metals chalcogenides, like for instance  $\text{MoSe}_2$  single-layer, where the gap change is attributed to phonon softening<sup>27</sup>. Intriguingly also for  $\text{CH}_3\text{NH}_3\text{PbI}_3$  we observe some softening of our calculated low-energy optical phonon modes, when the methyl-ammonium molecule rotates along the  $(0\pm 11)$  directions. In particular the calculated energy red shift is of the order of  $10 \text{ cm}^{-1}$  (see Supplementary Material: Fig. 5).

We have carefully verified that the indirect bandgap is not an artifact of our computation method. Firstly, we analyzed the relaxation in a  $2 \times 2 \times 2$  (96 atoms) supercell to establish whether further low-symmetry configurations are possible. The supercell converged geometries are very similar to the unit cell geometries repeated in space due to periodic boundary conditions. The calculations reveal no particular changes, although the size of the supercell would allow the  $\text{PbI}_6$  octahedra to rotate or tilt, in the octahedral tilt and rotation angles.

Consequently, the features of the bandgaps are preserved both at the qualitative as well as quantitative level. Secondly, we have tested different vdW functionals by comparing the geometries obtained with the Tkatchenko-Scheffler scheme<sup>21</sup> to those calculated with the empirical Grimme’s corrections<sup>28</sup>. We also performed single-point calculations employing a more sophisticated many-body dispersion (MBD) corrections<sup>29</sup>, on our relaxed geometries and did not find any significant change in the total energies. This suggests that TS and the Grimme’s pairwise dispersion methods give sufficiently good description for our system as found in a recent work for some molecular crystals<sup>30</sup>. The two methods return rather similar structures, both sustaining the indirect gap. Then, we have performed calculations using the HSE06<sup>31</sup> screened hybrid functional by starting from the optimal relaxed structures. Also in this case the bandgap remains indirect (see Supplementary Material: Fig. 3), although the overall energy distance between the CBM and the VBM increases, as expected, when the hybrid HSE06 functional is used. Finally, we verified that the indirect bandgap found for the  $\text{CH}_3\text{NH}_3$  along the  $(0\pm 11)$  directions survives to the inclusion of spin-orbit interaction. In this case, for the  $(0-11)$  orientation of the molecule, for example we notice that the VBM shifts away from the high symmetry R point, as reported in previous studies<sup>10,11</sup>. However, the CBM shifts of the same amount and along the same direction in the Brillouin zone thus that the indirect bandgap remains essentially untouched (see Supplementary Material: Fig. 4).

Recently, Mosconi et al.<sup>32</sup> published their work using Car-Parinello molecular dynamics (CPMD) results on a  $2\times 2\times 2$  supercell of  $\text{CH}_3\text{NH}_3\text{PBI}_3$  simulated at 319K showing a variation of  $\pm 0.1-0.2$  eV of the HOMO expected to affect the band gap as well. However, the nature of the gap was not analyzed. Not only this paper gives evidence that the size of the band gap is changing as function of the MA rotation, as we show here, but also underlines the importance of the effect we are reporting about the direct to indirect gap transition. However tracking the changes in the NATURE of the band gap as function of dynamic motion of the  $\text{CH}_3\text{NH}_3$  groups during CPMD simulation can be very tricky. For simplification, we restricted our study to few possible orientations of the molecule which is a considerable step forward with respect to existing literature, where essentially only one configuration (higher in energy) was explored. It would be of great interest to look at more complex dynamical effects, by taking snapshots of more  $\text{CH}_3\text{NH}_3$  orientations.

We also performed NEB calculation to evaluate the MA reorientation barrier from  $(011)$  to  $(111)$  taking into account the changes in cell geometry and lattice vectors. We found a barrier of 20 meV (1.929 KJ/mol) which is less than  $k_{BT}$  at room temperature,  $k_B$  is Boltzmann constant and  $T$  is the temperature, thus confirming our proposal of fast rotation above room temperature. This also suggest that at lower temperatures the MA 110 ori-

entation might be favored, a finding that could be confirmed using CPMD simulations and experiments. Worth noting that Forst et al.<sup>33</sup> reported a rotation barrier for MA and other molecules using PBEsol in VASP keeping the cubic lattice constants obtaining an upper, unrelaxed, limit of the rotation barrier of 13 meV ( 1.3 kJ/mol).

### Optical absorption

In order to seek further evidence of the presence of the indirect bandgap, we have calculated the perovskite’s optical absorption and compared it with available experimental data. The calculations have been performed over the electronic structure obtained with the PBE including vdW interaction in the independent particle approximation and without spin-orbit coupling. Although the fortuitous cancellation of errors returns a bandgap close to experiments, we concentrate here on the shape of the spectrum around the absorption edge. The calculations are performed for the three possible orientations of the  $\text{CH}_3\text{NH}_3$  molecule, namely  $(111)$ ,  $(011)$  and  $(0-11)$  and the various spectra are presented in Fig. 3(c).

When the methyl-ammonium molecule is aligned along the  $(111)$  direction the bandgap is direct and measures 1.423 eV=871 nm. The absorption profile then increases monotonically from that value, indicating the possibility of direct transitions across the band edges. In contrast, when  $\text{CH}_3\text{NH}_3$  is placed along  $(011)$  or  $(0-11)$ , then the bandgap is indirect, and in general slightly larger than that along  $(111)$ . In particular for  $(0-11)$  we find a direct gap of 1.611 eV = 769 nm and an indirect one of 1.629 eV = 761 nm, while for  $(011)$  the direct gap is 1.594 eV = 777 nm and the indirect one is 1.681 eV = 737 nm. In these two cases the shape of the absorption spectrum is quite different from the  $(111)$  case. Notably the two transverse orientations,  $(011)$  and  $(0-11)$ , show a rather similar absorption profile around the low energy region, so that they can be hardly distinguished. Differences between the two appear only at wavelengths around 650 nm and lower, i.e. away from the band edges. There is ‘two-step’ absorption profile (see the inset of fig 3(c)) with a small absorption amplitude developing at the band edge followed by a significantly more pronounced increase at around 750 nm. This reflects the indirect nature of the bandgap, and the fact that indirect transitions are not allowed, unless when assisted by phonons.

Certainly the level of theory used here is not complete, however the inclusion of excitonic effects is not necessary to make our main point about the shape of the spectrum around the absorption edge. Certainly a fully quantitative picture cannot be presented using our level of theory, but the difference between the direct and indirect band-gap are very evident from the inset of Fig. 3(c). Very recently, accurate absorption spectra computed using GW/BSE approach were published by Even et al.<sup>34</sup>, using cubic supercells with the MA oriented along 100

reproduced efficiently the experimentally measured excitonic effects appearing below the optical band gap. An example of experimental absorption spectrum measured at 300K is given SI: Fig 6 featuring a small amplitude around the bandgap followed by a rapid increase after about 50 nm which seems to be a robust feature in the experimentally measured spectra, regardless of the morphology of the material<sup>7,19,35</sup> and resistant to film quality degradation<sup>36</sup>.

However, since it is well known that at 300K the MA is dynamically rotating sampling the (011) and (111) family of orientations, among others, it is normal not to observe experimentally any neat indirect band gap, but rather absorption spectra starting around the average value of the band gap. This is a common finding among the experimental community working in the field. To complete the picture, we point out that our finding could help explaining the recently observed line broadening in photoluminescence experiments<sup>37</sup>, attributed to coupling with phonons. In fact, low energy phonons are associated with cation rotations, which in turn would shift the CBM to different positions. As a result, the range of optical gap would change as function of temperature thus broadening the emission spectrum. Measurement of the optical absorption and thermal characteristics using very high sensitivity techniques such as photothermal deflection spectroscopy might reveal the existence of the indirect band gap by fine lowering of temperature below 300K thus freezing the MA (111) family of orientations.

## DISCUSSION

As known, the main concept of the solar cells is to absorb photons and convert their energy to electrical form through photogenerated current with some gained voltage. For the first part, stronger absorbers are preferred, which is characterized by  $L_\alpha$  inversely proportional to the absorption<sup>38,39</sup>. For the second part (*i.e.* generating current), there are many parameters that contribute to it such as the mobility, the carrier lifetime, the carrier concentration, etc.. It is generally characterized by the carrier diffusion length ( $L_{diff}$ ) which is a measure of the mean distance that an excited carrier can diffuse before recombining.<sup>40-42</sup>  $L_{diff}$  is directly proportional to carrier lifetime ( $\tau$ ). For solar cells, it is essential to fulfil the condition on the ratio  $r=L_{diff}/L_\alpha > 1$  to ensure that the photogenerated carriers can be extracted and collected. For practical reasons, the ratio should be much larger than 1<sup>38-40,43</sup> to ensure a high power conversion efficiency (PCE).

Generally, direct band gap semiconductors, such as GaAs have better absorption and thus shorter  $L_\alpha$ , but this generally comes with faster carrier recombination and hence relatively smaller  $L_{diff}$ . The situation is the opposite for indirect band gap semiconductors such as silicon. However, a preferable balance between  $L_\alpha$  and  $L_{diff}$  for solar cells<sup>39</sup> is present in some indirect band gap

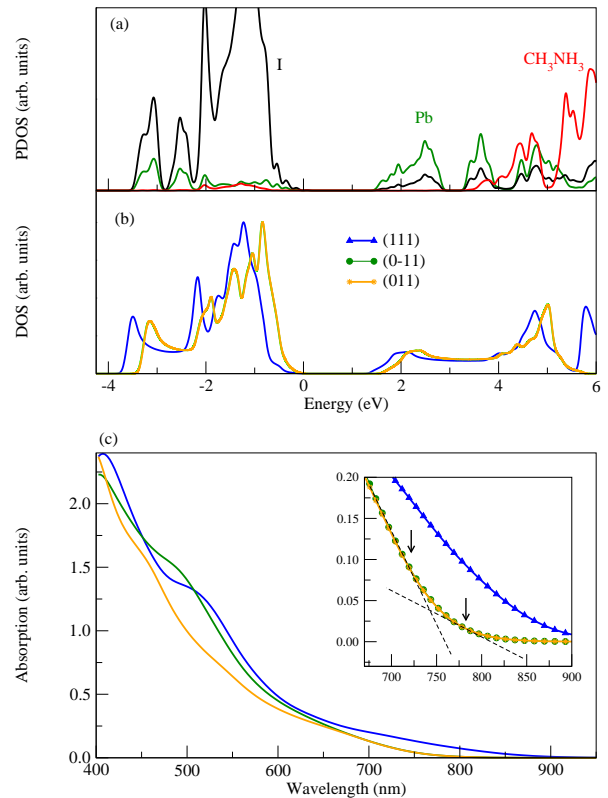


FIG. 3. Electronic and optical properties of the cubic phase  $\text{CH}_3\text{NH}_3\text{PBI}_3$ . In panel (a) we present the projected density of states for the case of the (111) oriented molecule on the Pb (green), I (black) species and the  $\text{CH}_3\text{NH}_3$  (red). In panel (b) we display the density of states as a function of the chemical potential for the molecule oriented along (111) (0-11) and (011) directions. In panel (c) the calculated absorption spectra are plotted for the different orientation of  $\text{CH}_3\text{NH}_3$  clearly showing the impact the organic cation rotation. The inset in (c) is a magnification of the same quantity around the low-energy region.

semiconductors such as  $\text{Cu}_3\text{N}$ <sup>40</sup>, where the direct transition starts few  $k_B T$  above the indirect gap, offering a short  $L_\alpha$ . The small difference between the indirect gap and the lowest direct transition ensures that the absorption is not greatly affected by the indirect gap till the direct transitions start dominating the absorption spectrum. On the other hand, the lifetime ( $\tau$ ) of the photogenerated carriers which relax to the band edges in the indirect gap is longer than that of the direct gap by orders of magnitudes<sup>41</sup> ensuring a large  $L_{diff}$ . This class of indirect semiconductors promise remarkable improvement of PCE via enhancement of the ratio between  $L_{diff}$  and  $L_\alpha$ <sup>39,40</sup>.

With these results at hand we can speculate on the possible origin of the high efficiency in hybrid perovskites solar cells. Density functional theory calculations, including vdW interactions, has allowed us to establish that, under certain conditions of molecule alignment, the bandgap of the high-temperature phase of  $\text{CH}_3\text{NH}_3\text{PBI}_3$

can be indirect and not always direct as previously believed. This feature originates from the strain exerted on the  $\text{PbI}_6$  octahedra by the organic molecules, when these align along the (011) or (0-11) directions, which constitute shallow minima in the total energy profile. The indirect bandgap is several tens of meV smaller than the direct one and the position of the conduction band minimum with respect to the valence band maximum depends on the specific orientation of the molecules. This analysis delivers a picture of  $\text{CH}_3\text{NH}_3\text{PbI}_3$  as a “dynamical” bandgap semiconductor, where the term “dynamical” refers to the fact that the position in  $k$ -space of the conduction band minimum depends on the molecular alignment, which in turn fluctuates at room temperature. The calculated absorption spectrum near the band edge, characterized by a shallow amplitude at about 800 nm followed by a rapid enhancement within 50 nm, is very similar for the two equivalent orientations of the molecules (011) and (0-11), indicating that it is a feature robust to the molecular rotation and disorder.

The presence of an indirect bandgap, with only a small displacement in  $k$ -space with respect to the direct point, suggests that the rapid relaxation of the photo-excited electrons to the conduction band minimum is still possible. This process is incoherent, mediated by acoustic phonons, and spontaneously breaks the excitons in free carriers. As a second effect of the collapse of the electrons to the indirect conduction band minimum is that the lifetime of the minority carriers is enhanced, so that radiative recombination is partially suppressed. Such suppression is not complete since experiments reveal luminescence, however it contributes to prolong the carrier lifetime ( $\tau$ ). In fact it is interesting to note that experiments reported that the luminescence gets suppressed as the material crystallizes<sup>35</sup> and that in any case it is sensitive to the sample morphology and quality<sup>44</sup>. Considering that the crystallization process leads to the geometries described here, such suppression of the luminescence upon ordering supports our argument. To complete the picture it is also worth reminding that the absence of strong scattering centers inhibits incoherent recombination, so that  $L_{\text{diff}}$  remains long<sup>45</sup>.

## CONCLUSIONS

Despite the tremendous advances in studying and understanding hybrid perovskites from both the theoretical and the experimental point of views, yet the reason behind the extended carrier lifetime in these materials remains a mystery. This work suggests that extended carrier lifetimes in  $\text{CH}_3\text{NH}_3\text{PbI}_3$  might be a consequence of the “dynamical” position of the conduction band minimum forming a basin around a high symmetry point in the  $k$ -space. This proposed dynamical band gap, induced by the molecular motion, prohibits carrier recombination, favors exciton separation thus increasing the conversion efficiency of the photovoltaic absorber  $\text{CH}_3\text{NH}_3\text{PbI}_3$ .

Crucially, all such phenomenology appears to be initiated by the geometry assumed by the molecules following full geometry relaxation. A set of differently oriented  $\text{CH}_3\text{NH}_3$  cations geometries were relaxed without any symmetry constrains using density functional theory including van der Waals forces lead to geometries where the  $\text{PbI}_6$  octahedra distort. The band-structure corresponding to such geometry presents an indirect band-gap which persists upon bandgap corrections via screened hybrid functionals and spin-orbit coupling. Finally, we propose that a possible way for engineering the efficiency of hybrid perovskites is to induce distortion to the  $\text{PbI}_6$  octahedra either by using strain or organic molecules strongly interacting with the inorganic cages.

## ACKNOWLEDGMENTS

This work is sponsored by the European Research Council, QUEST project, (CM and SS) and by the Qatar Environment and Energy Research Institute (FE, FHAH, NT and SK). Computational resources have been provided by the supercomputer facilities at the Trinity Center for High Performance Computing, at ICHEC (project tephy038b) and the research computing at Texas A&M University at Qatar. We acknowledge fruitful discussions with Simon Gelinas, Marcelo Carignano and Mohamed Lamine Madjet and thank Felix Deschler for sending his absorption spectra.

## COMPUTATIONAL DETAILS

### DFT calculations

The electronic properties of the hybrid perovskites have been calculated with the all-electron FHI-AIMS code at the level of GGA in the Perdew-Burke-Ernzerhof (PBE)<sup>20</sup> parameterization. Long-range van der Waals interactions have been taken into account via the Tkatchenko and Scheffler (TS) scheme<sup>21</sup>, which is also constructed over a GGA and a pairwise dispersive potential. The reciprocal space integration was performed over an  $8 \times 8 \times 8$  Monkhorst-Pack grid<sup>46</sup>. A pre-constructed high-accuracy all-electron basis set of numerical atomic orbitals was employed, as provided by the FHI-AIMS “tight” default option (more details are given in SI ). Unconstrained structural optimization was performed with the Broyden-Fletcher-Goldfarb-Shanno algorithm<sup>47</sup>, with a tolerance of  $10^{-3}$  eV/Å and with the constraint of orthogonal cell vectors.

Additional calculations, in particular concerning the use of the hybrid functional HSE06<sup>31</sup>, were performed using the GAUSSIAN suite<sup>48</sup>, with the periodic boundary condition<sup>49</sup> code version. The Def2-<sup>50</sup> series of GAUSSIAN basis sets were optimized following our own procedure, described in Ref. [51], for the atomic species of interest in this work. Most numerical settings in GAUSSIAN were left at the default values, *e.g.*, unconstrained ge-

ometry optimization settings, integral cut-offs, and self-consistent convergence thresholds. The standard rms force threshold in GAUSSIAN for geometry optimizations is  $450 \times 10^{-6}$  hartrees/bohr. The default  $k$ -point mesh of  $8 \times 8 \times 8$  was used for the 12 atoms unit cell of  $\text{CH}_3\text{NH}_3\text{PbI}_3$ .

Finally calculations involving the spin-orbit interaction have been carried out by using the QUANTUM ESPRESSO package<sup>52</sup>. Electron-ion interaction were described by scalar relativistic ultra-soft pseudopotentials. An  $8 \times 8 \times 8$  Monkhorst-Pack grid<sup>46</sup> was adopted and plane-wave cut-offs of 40 and 400 Ry were chosen for the wavefunction and the density, respectively.

The linear optical absorption has been obtained with

FHI-AIMS by computing the momentum matrix elements in a 5 eV energy window around the Fermi level and then by using the Fermi golden rule approximation. A dense  $k$ -point sampling of  $15 \times 15 \times 15$  has been employed to ensure converged spectra.

### Phonon calculations

Phonons spectra were computed with the frozen-phonon approach for a fully relaxed  $2 \times 2 \times 2$  supercells using the Phonopy<sup>53</sup> code in combination with FHI-AIMS. A displacement of 0.001 Å was applied to each atom in the three space directions to compute the dynamical matrix. The phonon density of states used the  $\Gamma$  point sampling while the full phonon band structure was generated using the  $\Gamma$ ,  $M$ ,  $X$  and  $R$  high symmetry points in the Brillouin zone.

- 
- \* mottac@tcd.ie  
 † felmellouhi@qf.org.qa
- <sup>1</sup> H. J. Snaith, The Journal of Physical Chemistry Letters **4**, 3623 (2013)
  - <sup>2</sup> P. P. Boix, K. Nonomura, N. Mathews, and S. G. Mhaisalkar, Materials Today **17**, 16 (2014)
  - <sup>3</sup> M. A. Loi and J. C. Hummelen, Nature Materials **12**, 1087 (2013)
  - <sup>4</sup> F. Deschler, M. Price, S. Pathak, L. E. Klintberg, D.-D. Jarausch, R. Higler, S. Hüttner, T. Leijtens, S. D. Stranks, H. J. Snaith, M. Ataiüre, R. T. Phillips, and R. H. Friend, The Journal of Physical Chemistry Letters, 1421(2014)
  - <sup>5</sup> E. Mosconi, A. Amat, M. K. Nazeeruddin, M. Grätzel, and F. De Angelis, The Journal of Physical Chemistry C **117**, 13902 (2013)
  - <sup>6</sup> M. Liu, M. B. Johnston, and H. J. Snaith, Nature **501**, 395 (2013)
  - <sup>7</sup> G. Xing, N. Mathews, S. Sun, S. S. Lim, Y. M. Lam, M. Grätzel, S. Mhaisalkar, and T. C. Sum, Science **342** (2013)
  - <sup>8</sup> W.-J. Yin, T. Shi, and Y. Yan, Applied Physics Letters **104**, (2014)
  - <sup>9</sup> J. Kim, S.-H. Lee, J. H. Lee, and K.-H. Hong, The Journal of Physical Chemistry Letters, 1312(2014)
  - <sup>10</sup> F. Brivio, K. T. Butler, A. Walsh, and M. van Schilfgaarde, Phys. Rev. B **89**, 155204 (2014)
  - <sup>11</sup> P. Umari, E. Mosconi, and F. De Angelis, Scientific Reports **4** (2014)
  - <sup>12</sup> T. Baikie, Y. Fang, J. M. Kadro, M. Schreyer, F. Wei, S. G. Mhaisalkar, M. Grätzel, and T. J. White, Journal of Materials Chemistry A **1**, 5628 (2013)
  - <sup>13</sup> O. Knop, R. E. Wasylshen, M. A. White, T. S. Cameron, and M. J. M. V. Oort, Canadian Journal of Chemistry **68**, 412 (1990)
  - <sup>14</sup> Y. Wang, T. Gould, J. F. Dobson, H. Zhang, H. Yang, X. Yao, and H. Zhao, Physical Chemistry Chemical Physics **16**, 1424 (2014)
  - <sup>15</sup> J. Even, L. Pedesseau, J.-M. Jancu, and C. Katan, The Journal of Physical Chemistry Letters **4**, 2999 (2013)
  - <sup>16</sup> J. Even, L. Pedesseau, J.-M. Jancu, and C. Katan, physica status solidi (RRL) Rapid Research Letters **8**, 31 (2014)
  - <sup>17</sup> J. Feng and B. Xiao, The Journal of Physical Chemistry Letters **5**, 1278 (2014)
  - <sup>18</sup> G. Giorgi, J.-I. Fujisawa, H. Segawa, and K. Yamashita, The Journal of Physical Chemistry C **118**, 12176 (2014)
  - <sup>19</sup> M. M. Lee, J. Teuscher, T. Miyasaka, T. N. Murakami, and H. J. Snaith, Science **338**, 643 (2012)
  - <sup>20</sup> J. P. Perdew, K. Burke, and M. Ernzerhof, Phys. Rev. Lett. **77**, 3865 (1996)
  - <sup>21</sup> A. Tkatchenko and M. Scheffler, Phys. Rev. Lett. **102**, 073005 (2009)
  - <sup>22</sup> A. Poglitsch and D. Weber, The Journal of Chemical Physics **87**, 6373 (1987)
  - <sup>23</sup> F. Brivio, A. B. Walker, and A. Walsh, APL Materials **1**, (2013)
  - <sup>24</sup> C. C. Stoumpos, C. D. Malliakas, and M. G. Kanatzidis, Inorganic Chemistry **52**, 9019 (2013)
  - <sup>25</sup> A. Kojima, K. Teshima, Y. Shirai, and T. Miyasaka, Journal of the American Chemical Society **131**, 6050 (2009)
  - <sup>26</sup> F. El-Mellouhi, E. N. Brothers, M. J. Lucero, I. W. Bulik, and G. E. Scuseria, Physical Review B **87**, 035107 (2013)
  - <sup>27</sup> S. Horzum, H. Sahin, S. Cahangirov, P. Cudazzo, A. Rubio, T. Serin, and F. M. Peeters, Phys. Rev. B **87**, 125415 (2013)
  - <sup>28</sup> S. Grimme, Journal of Computational Chemistry **27** (2006)
  - <sup>29</sup> A. Tkatchenko, R. A. DiStasio, R. Car, and M. Scheffler, Phys. Rev. Lett. **108**, 236402 (2012)
  - <sup>30</sup> L. Kronik and A. Tkatchenko, Accounts of Chemical Research (2014)
  - <sup>31</sup> A. V. Krukau, O. A. Vydrov, A. F. Izmaylov, and G. E. Scuseria, The Journal of Chemical Physics **125** (2006)
  - <sup>32</sup> E. Mosconi, C. Quarti, T. Ivanovska, G. Ruani, and F. De Angelis, Physical Chemistry Chemical Physics (2014)
  - <sup>33</sup> J. M. Frost, K. T. Butler, F. Brivio, C. H. Hendon, M. van Schilfgaarde, and A. Walsh, Nano Letters **14**, 2584 (2014)
  - <sup>34</sup> J. Even, L. Pedesseau, and C. Katan, The Journal of Physical Chemistry C **118**, 11566 (2014)
  - <sup>35</sup> J. Burschka, N. Pellet, S.-J. Moon, R. Humphry-Baker, P. Gao, M. K. Nazeeruddin, and M. Grätzel, Nature **499**, 316 (2013)
  - <sup>36</sup> G. Niu, W. Li, F. Meng, L. Wang, H. Dong, and Y. Qiu, Journal of Materials Chemistry A **2**, 705 (2014)
  - <sup>37</sup> C. Wehrenfennig, M. Liu, H. J. Snaith, M. B. Johnston, and L. M. Herz, The Journal of Physical Chemistry Letters **5**, 1300 (2014)

- <sup>38</sup> J. J. Loferski, *Journal of Applied Physics* **27**, 777 (1956)
- <sup>39</sup> F. Alharbi, J. D. Bass, A. Salhi, A. Alyamani, H.-C. Kim, and R. D. Miller, *Renewable Energy* **36**, 2753 (2011)
- <sup>40</sup> A. Zakutayev, C. M. Caskey, A. N. Fioretti, D. S. Ginley, J. Vidal, V. Stevanovic, E. Tea, and S. Lany, *The Journal of Physical Chemistry Letters* **5**, 1117 (2014)
- <sup>41</sup> S. Fonash, *Solar Cell Device Physics* (Oxford: Academic Press, 2010)
- <sup>42</sup> M. Law, E. Solley, M. Liang, and D. Burk, *Electron Device Letters*, *IEEE* **12**, 401 (1991)
- <sup>43</sup> M. Grätzel, *Nature* **414**, 338 (2001)
- <sup>44</sup> J. J. Choi, X. Yang, Z. M. Norman, S. J. L. Billinge, and J. S. Owen, *Nano Letters* **14**, 127 (2013)
- <sup>45</sup> S. D. Stranks, G. E. Eperon, G. Grancini, C. Menelaou, M. J. P. Alcocer, T. Leijtens, L. M. Herz, A. Petrozza, and H. J. Snaith, *Science* **342**, 341 (2013)
- <sup>46</sup> H. J. Monkhorst and J. D. Pack, *Phys. Rev. B* **13**, 5188 (1976)
- <sup>47</sup> W. H. Press, S. A. Teukolsky, W. T. Vetterling, and B. P. Flannery, *Numerical recipes*, 3rd ed. (Cambridge University Press, 1997)
- <sup>48</sup> M. J. Frisch, G. W. Trucks, H. B. Schlegel, G. E. Scuseria, M. A. Robb, J. R. Cheeseman, G. Scalmani, V. Barone, B. Mennucci, G. A. Petersson, H. Nakatsuji, M. Caricato, X. Li, H. P. Hratchian, A. F. Izmaylov, J. Bloino, G. Zheng, J. L. Sonnenberg, M. Hada, M. Ehara, K. Toyota, R. Fukuda, J. Hasegawa, M. Ishida, T. Nakajima, Y. Honda, O. Kitao, H. Nakai, T. Vreven, J. A. Montgomery, Jr., J. E. Peralta, F. Ogliaro, M. Bearpark, J. J. Heyd, E. Brothers, K. N. Kudin, V. N. Staroverov, R. Kobayashi, J. Normand, K. Raghavachari, A. Rendell, J. C. Burant, S. S. Iyengar, J. Tomasi, M. Cossi, N. Rega, J. M. Millam, M. Klene, J. E. Knox, J. B. Cross, V. Bakken, C. Adamo, J. Jaramillo, R. Gomperts, R. E. Stratmann, O. Yazyev, A. J. Austin, R. Cammi, C. Pomelli, J. W. Ochterski, R. L. Martin, K. Morokuma, V. G. Zakrzewski, G. A. Voth, P. Salvador, J. J. Dannenberg, S. Dapprich, A. D. Daniels, o. Farkas, J. B. Foresman, J. V. Ortiz, J. Cioslowski, and D. J. Fox, "Gaussian 09 revision {B}.01," Gaussian Inc. Wallingford CT 2009
- <sup>49</sup> K. N. Kudin and G. E. Scuseria, *Phys. Rev. B* **61**, 16440 (2000)
- <sup>50</sup> F. Weigend and R. Ahlrichs, *Phys. Chem. Chem. Phys.* **7**, 3297 (2005)
- <sup>51</sup> F. El-Mellouhi, E. N. Brothers, M. J. Lucero, and G. E. Scuseria, *Phys. Rev. B* **84**, 115122 (2011)
- <sup>52</sup> P. Giannozzi, S. Baroni, N. Bonini, M. Calandra, R. Car, C. Cavazzoni, D. Ceresoli, G. L. Chiarotti, M. Cococcioni, I. Dabo, A. Dal Corso, S. de Gironcoli, S. Fabris, G. Fratesi, R. Gebauer, U. Gerstmann, C. Gougousis, A. Kokalj, M. Lazzeri, L. Martin-Samos, N. Marzari, F. Mauri, R. Mazzarello, S. Paolini, A. Pasquarello, L. Paulatto, C. Sbraccia, S. Scandolo, G. Sciauzero, A. P. Seitsonen, A. Smogunov, P. Umari, and R. M. Wentzcovitch, *J. Phys.: Condens. Matter* **21**, 395502 (2009)
- <sup>53</sup> A. Togo, F. Oba, and I. Tanaka, *Phys. Rev. B* **78**, 134106 (2008)

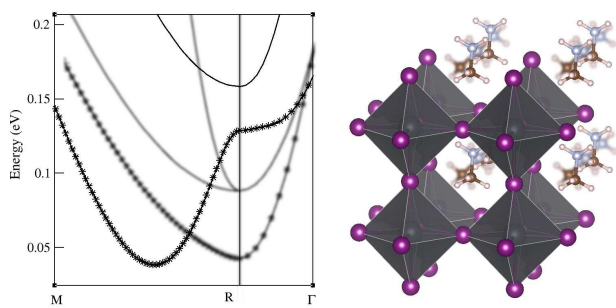


FIG. 4. Cover Picture